scientific reports

Check for updates

OPEN

Image-processing-based model for surface roughness evaluation in titanium based alloys using dual tree complex wavelet transform and radial basis function neural networks

J. S. Vishwanatha[1], P. Srinivasa Pai[1], Grynal D'Mello[1], L. Sampath Kumar[2], Raghavendra Bairy[3], Madeva Nagaral[4]✉, N. Channa Keshava Naik[5]✉, Venkatesh T. Lamani[6], A. Chandrashekar[7], T. M. Yunus Khan[8], Naif Almakayeel[9] & Wahaj Ahmad Khan[10]✉

In this study, we examine the assessment of surface roughness on turned surfaces of Ti 6Al 4V using a computer vision system. We utilize the Dual-Tree Complex Wavelet Transform (DTCWT) to break down the images of the turned surface into sub-images oriented in directions. Three different methods of feature generation have been compared, i.e., the use of Gray-Level Co-Occurrence Matrix (GLCM) and DTCWT-based extraction of second-order statistical features, DTCWT Image fusion, and the use of GLCM for feature extraction, and DTCWT image fusion using Particle Swarm Optimization (PSO) based GLCM features. Principal Component Analysis (PCA) was utilized to identify and select features. The model was developed using a Radial Basis Function Neural Network (RBFNN). Accordingly, six models were designed based on the three feature generation methods, considering all features and features selected using PCA. The RBFNN model, which incorporates DTCWT Image fusion and utilizes PSO with PCA features, achieved a training data prediction accuracy of 100% and a test data prediction accuracy of 99.13%.

Keywords PSO, PCA, DTCWT, RBFNN, GLCM, Computer vision

The primary requirement for customers in the machining method is a prediction of surface roughness that affects the components' efficiency and the production cost. All manufacturing firms remove material from workpieces using different production methods. Turning is a widely used metal removal method due to its faster metal removal rate and reasonable surface quality compared to other methods. Surface roughness refers to the measurement of irregularities that are created during the machining process[1]. Titanium alloys are still considered as hard-to-machine materials[2]. The poor machinability of titanium makes it difficult for machining. It is observed that poor machinability is due to relatively lower thermal conductivity, higher strength even at very high temperatures, and increased chemical reactivity, resulting in poor surface finish[3].

[1]Department of Mechanical Engineering, NMAM Institute of Technology, NITTE (Deemed to be University), Nitte, Karnataka 574110, India. [2]Department of Mechanical Engineering, Sir MVIT, Bengaluru, Karnataka 562157, India. [3]Department of Biotechnology Engineering. NMAM Institute of Technology, NITTE (Deemed to be University), Nitte, Karnataka 574110, India. [4]Aircraft Research and Design Centre, Hindustan Aeronautics Limited, Bangalore, Karnataka 560037, India. [5]Department of Mechanical Engineering, BGS College of Engineering and Technology, Bangalore, Karnataka 560086, India. [6]Department of Mechanical Engineering, BMS College of Engineering, Bangalore, India. [7]Department of Mechanical Engineering, Bangalore Institute of Technology, 560004 Bengaluru, India. [8]Department of Mechanical Engineering, College of Engineering, King Khalid University, Abha 61421, Saudi Arabia. [9]Department of Industrial Engineering, King Khalid University Abha Saudi Arabia, Abha, Saudi Arabia. [10]School of Civil Engineering and Architecture, Institute of Technology, Dire-Dawa University, 1487 Dire Dawa , Ethiopia. ✉email: madev.nagaral@gmail.com; naikphd.sit@gmail.com; wkhan9450@gmail.com

Surface roughness can be measured using two approaches: contact and non-contact methods. The contact method involves using devices that directly touch the surface being measured. On the other hand, the non-contact method utilizes convenient devices for automation[4]. It has several advantages compared with contact methods[4,5]. Therefore, researchers have widely focused their interest in this approach. Using computer vision, Lee and Tarng[4] predicted surface roughness in turned images of parts. To anticipate the roughness of a surface, authors employed a self-organizing model to establish the connection between extracted characteristics and the actual surface roughness. Patricia Morala Argüello et al.[6] presented a technique to predict the roughness of twisted surfaces in their study. The wavelet transform was applied to extract features and subsequently employed as input for a propagation neural network to forecast surface roughness.

Several researchers have used image-processing techniques to evaluate turned workpieces surface roughness[7]. The most popular multi-resolution or multichannel analysis method for textural analysis is wavelet transform. The wavelet transform is known for its ability to effectively retain the information of signals in both the time domain and the frequency domain. Hence, it efficiently extracts meaningful features from the images[8]. Many researchers have used discrete wavelet transform (DWT) and other combined approaches to extract meaningful features. Even though DWT is effectively used in image processing, it has disadvantages like lack of directionality, shift variance, and aliasing[9]. DTCWT provides shift invariance and better directionality than DWT. Regarding the analysis and synthesis of textural images, DTCWT has proven to perform better than all other wavelet transforms[10]. The relevance of DTCWT in image fusion lies in its advantages[11]. Typically, the low-frequency coefficients obtained from decomposition are fused using the fusion rule for image fusion. However, this approach often alters the image intensity, diminishing the contrast of the resulting combined image. The low-frequency coefficients are fused using region-based image fusion to avoid these disadvantages. Using an optimization technique in region-based image fusion can enhance the performance of the image fusion process. Many researchers have used PSO to optimize the machining conditions. PSO algorithm has proven its potential in chatter recognition through vibration signals with wavelet packet transform during milling operation[12]. PSO-optimized machining parameters resulted in better-machined surfaces for shape memory alloys[13] and steels[14] than other algorithms. PSO is applied to increase the image segmentation efficiency to locate defects in printed circuit boards[15]. PSO-optimized multiple responses produced better efficiency in the electric discharge machining process[16]. PSO method yielded better outcomes in application and objective performance when compared to more recent image fusion techniques[17,18].

Many researchers have primarily concentrated on extracting characteristics from images of machined surfaces. The purpose is to establish a correlation between the extracted features and the roughness of these surfaces[19]. However, when conducting an analysis, it is essential to consider the individual gray-level values of image pixels and spatial relationships. The order characteristics are extracted using the GLCM approach. The GLCM method involves tabulating the occurrence of combinations of brightness values within an image. Gadelmawla[20] proposed an approach to surface roughness analysis of captured images of lapped and flat copper specimens using GLCM-based imaging techniques. Bhat et al.[21] introduced a method for classifying tool wear states using support vector machines (SVM) with a kernel-based approach. They utilized features extracted from machined surface images through GLCM analysis.

In machining processes, predictive modeling has proved its worth as a beneficial tool, where the effectiveness of input variables can be evaluated concerning the output of the system[22]. Several researchers have achieved favorable results by employing multilayer perceptron networks (MLPNN) and the backpropagation technique to forecast surface roughness on twisted surfaces[23,24]. Tsai et al.[25] performed surface roughness classification of milled and shaped surfaces using the Fourier Transform and MLPNN model. In their study, Grynal et al.[26] investigated various modelling strategies to forecast the surface roughness of Ti-6Al-4 V speed-turned surfaces. The RBFNN model was found to perform better than the BPNN model and the RSM. Garg et al.[27] compared drill flank wear prediction using RBFNN with the BPNN model, and it was observed that the computational time required for RBFNN model is less than the BPNN model.

The DTCWT outperformed traditional surface analysis methods due to their reduced measurement time due to lesser environmental and measurement variability, effective noise filtration in a single measurement, maintaining actual surface features while filtering out the noise, and improved reliability[28,29]. Furthermore, DTCWT decomposes the signal into low and high-frequency components, enabling target noise filtration without affecting the surface parameters[30–32]. However, DTCWT possesses significant disadvantages, such as errors during signal reconstruction when using the universal threshold method for Gaussian noise[33,34]. Integrating DTCWT with PCA mitigates these errors by identifying and reducing the noise, leading to more accurate machined surface analysis[35]. GLCM's proven their potential to conduct a detailed texture analysis[36], noise reduction[37], improved feature extraction[38], and error mitigation in surface analysis. The significant advantages of DTCWT, PCA, GLCM and neural network models have led researchers to develop a novel hybrid technique for machined surface analysis. Note that very little research has been reported on surface roughness prediction using RBFNN modeling in Ti-6Al-4 V machined surfaces. No efforts have been made to use PSO to extract optimized GLCM features based on DTCWT image fusion and PCA to minimize Gaussian noise for modeling and prediction in machining applications, notably machining titanium-based alloys for surface roughness. In current work, an effort has been made to utilize GLCM-based features using DTCWT image fusion with PSO for surface roughness evaluation of Ti-6Al-4 V turned surfaces. Figure 1 gives the methodology adopted for the current work.

Experimental scheme and procedure

The details and procedures followed for the present work are summarized for carrying out experiments.

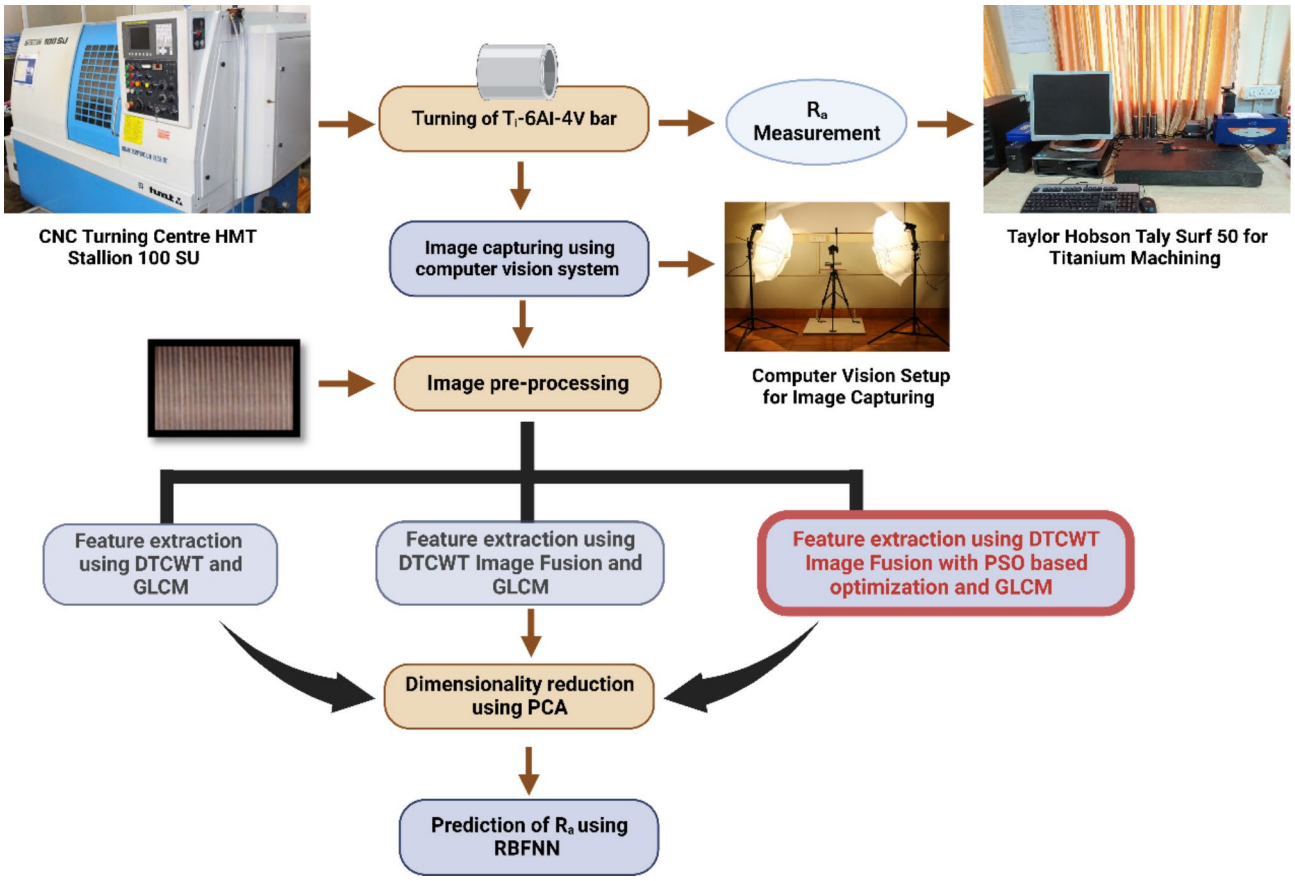

Fig. 1. Methodology adopted in this work.

CNC turning centre, cutting tool inserts and workpiece material

Turning experiments were conducted utilizing an HMT-made Stallion 100 SU CNC turning centre under dry cutting conditions. The turning centre has a continuously variable spindle drive with a 100–3500 rpm speed range. A manufacturer grade 883 with MR4 chip breaker (SECO make) coated carbide tool inserts and tool holder PCLNL 2020.

K12 (SECO make) is used for turning experiments. Table 1 provides more information regarding the machine equipment and tool inserts utilized. The turning tests utilize Ti-6Al-4 V round bars with a length of 200 mm and a diameter of 50 mm. The chemical composition of Ti-6Al-4 V has been presented in Table 2.

Experimental design

The Design of Experiments (DOE) methodology has been carried out using the statistical program MINITAB 17. The turning experiments have been conducted with 150, 175, and 200 m/min cutting speeds. The feed rates have been set at 0.15, 0.20, and 0.25 mm/rev, and the depth of cut (DOC) has been varied between 0.8, 1.0, and 1.2 mm. The most suitable DOE configuration is a 3^3 full factorial design with 27 machining tests. Table 3 presents the experimental design used in this study and its corresponding response. For measuring the arithmetic surface roughness data (R_a), the turned round bar is divided into three regions at 120° on the surface of the workpiece. The surface roughness is assessed at three distinct positions; the R_a value presented in Table 3 is the mean of three Ra measurements. The choice of these machining settings is derived from existing literature sources[26] and suggestions provided by the insert manufacturer. Hence, the experiments carried out replicate scenarios possible in a production environment. For these machining parameters, the range of R_a values varies from a minimum of 0.3910 to a maximum of 1.3852 µm. From the obtained $R_a$values for machining of Ti-6Al-4 V turned surfaces, it is established that rough turning operations have been carried out. The experimental setup is shown in Fig. 2.

Computer vision system

A rudimentary computer vision system has been devised to capture various rotated surface images. This system comprises a digital camera, a work table, and lighting setups. Round bars were positioned on a V-block fixture placed on a work table. An adjustable Tripod stand is to fix the camera; adjustable light stands have been used to illuminate it. The image capture process involved the using a Sony DSC H300 digital camera with a resolution of 20.1 Megapixels. The photos were acquired to acquire precise data from the images of the rotated surface. Image distortion can be rectified using a 35x optical zoom lens. The lens has a focal length range of 25–875 mm. A Super HAD CCD 1/2.3 type sensor can capture high-quality images with minimal noise distortion, even in

Machine tool (HMT make Stallion 100 SU CNC turning centre)	
Spindle motor power	5.5 kW
Maximum diameter of the turned shaft	250 mm
Maximum length of the turned shaft	460 mm
Speed range	100–3500 rpm
Number of tool stations	8
CNC system	FANUC OTD make
Tool insert (Coated carbide tool inserts 883 with MR4 chip breaker)	
Material	Carbide
Insert Style	CNMG
Insert Size	432
Manufacturer's Grade	883
Chip Breaker	MR4
Shape	Diamond
Inscribed Circle (mm)	12.7
Corner Radius (mm)	0.8
Coating	TiAlN
Insert Holding Method	Pin and Clamp

Table 1. Machine tool and Tool insert specifications.

Element	Ti	Al	V	C	O	*N*	H	Fe
% By Weight	90	6	4	< 0.10	< 0.20	< 0.05	< 0.0125	< 0.3

Table 2. Ti-6Al-4V chemical composition.

low-light conditions. A shutter speed of 1/200 seconds has been set. For the lighting arrangement, PLT Q50T3 48-watt clear double-ended two halogen bulbs have been used, which are placed approximately at an incidence angle of 45° concerning the specimen surface, and used in similar work[39]. Two optical white satin diffusion umbrellas have been used for uniform illumination using light. The purpose of maintaining a white background during picture acquisition is to minimize any distortion present in the collected images. The distance between the camera and the workpiece surface is essential to capture the necessary information about the surface topology. The optimal quality of the rotated surface images was achieved when the distance was roughly 25 cm. This configuration amplifies the attributes of surface patterns and bears a resemblance to the research conducted in[25]. Figure 3 shows the simple computer vision setup to capture turned surface images. The total experiments consisted of 461 machining passes, with each pass being 48 mm in length. For each pass, 3 images were captured at an angle of 120° on the circumference of the workpiece, resulting in a total of 1383 turned images for analysis.

The turned surface images are captured with 5152 × 3864 pixel resolution using a simple computer vision system. Figure 4a gives the actual captured turned surface image for cutting conditions: 200 m/min speed, feed 0.20 mm/rev and depth of cut 1.2 mm. The image area was selected from the captured images based on the best visual quality of the image. The captured images have been cropped to 256 × 256 pixels on the turned surface images using Picasa software before using it for image processing. This corresponds to approximately 9.5 × 9.5 $mm^2$of the specimen surface and has been considered based on similar work in the reference[39]. Figure 4b shows the cropped image to 256 × 256 resolution.

Measurement of surface roughness and tool flank wear

The average arithmetic surface roughness is the predominant surface finish characteristic utilized in industry and research[6]. The present work includes two types of surface roughness measurement: stylus-based measurement and computer vision system of measurement. The stylus measurement is regarded as a reference system, while the vision system is considered a proposed surface system measurement. A stylus-based Taylor Hobson Form Taly Surf 50 was used to measure the surface roughness. The sampling length is determined as per the recommended cut-off (ISO 4288-1996). Therefore, the sampling length in this study is 2.5 mm, while the evaluation length is 12.5 mm. Table 4; Fig. 5 give the specifications and setup for surface roughness measurement, respectively.

The tool flank wear is documented after each turning pass. After the completion of the measurement, the tool insert was reattached to the tool holder for additional machining. The process was continued until the tool's flank wear (VB_{max}) reached a maximum value of 0.4 mm. It is considered one of the input parameters for the RBFNN model. The tool wear rate varies for different cutting conditions.

Each cutting pass has been maintained for a constant distance of 48 mm. It is measured using Mitutoyo-made TM 505/510, a compact Tool Maker's Microscope. It has digital micrometer heads on the X and Y axis, which can

Exp. no.	Speed (m/min)	Feed (mm/rev)	DOC (mm)	Measured R_a (µm)
1	150	0.15	0.8	0.8337
2	150	0.20	0.8	1.3688
3	150	0.25	0.8	1.2584
4	175	0.15	0.8	0.5510
5	175	0.20	0.8	0.7025
6	175	0.25	0.8	0.9282
7	200	0.15	0.8	0.4703
8	200	0.20	0.8	1.3688
9	200	0.25	0.8	0.8172
10	150	0.15	1.0	0.6332
11	150	0.20	1.0	0.6407
12	150	0.25	1.0	0.6815
13	175	0.15	1.0	0.6455
14	175	0.20	1.0	0.5958
15	175	0.25	1.0	0.7572
16	200	0.15	1.0	0.3910
17	200	0.20	1.0	0.6224
18	200	0.25	1.0	0.7172
19	150	0.15	1.2	0.5109
20	150	0.20	1.2	0.6822
21	150	0.25	1.2	0.7491
22	175	0.15	1.2	0.4307
23	175	0.20	1.2	1.1371
24	175	0.25	1.2	0.9007
25	200	0.15	1.2	0.5133
26	200	0.20	1.2	1.3305
27	200	0.25	1.2	1.3852

Table 3. Design of experiment inputs and its response.

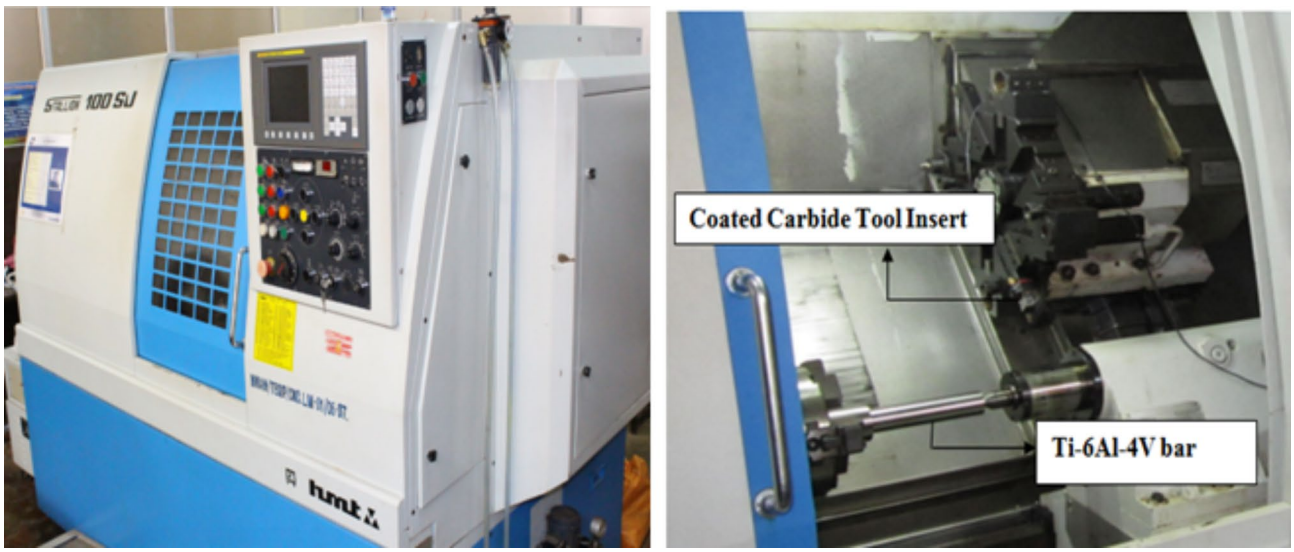

Fig. 2. (**a**) CNC Turning Centre HMT Stallion 100 SU. (**b**) Experimental setup.

Fig. 3. A simple computer vision setup for capturing turned images.

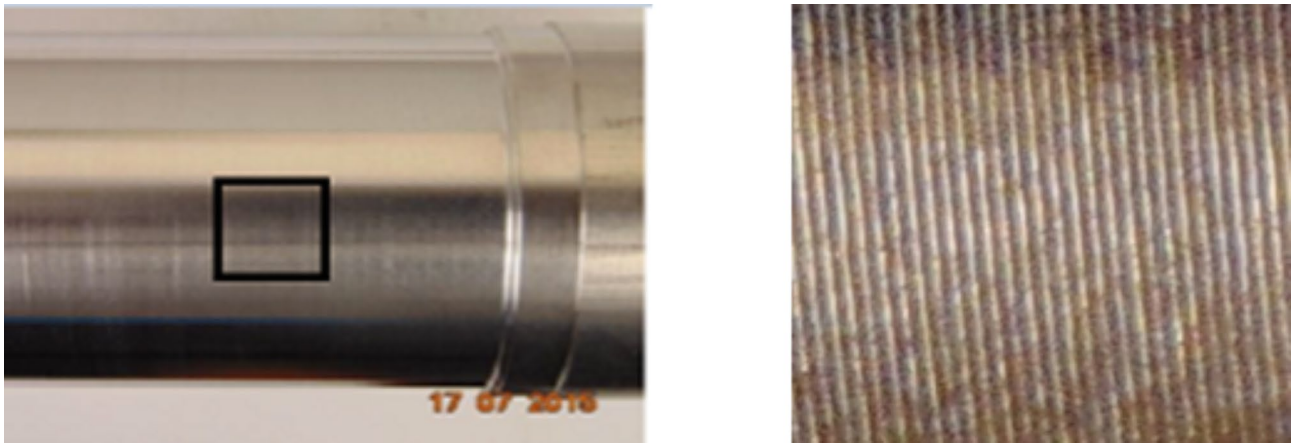

Fig. 4. (**a**) Actual turned image. (**b**) Cropped image to 256 × 256 resolution.

measure a negligible value of 0.005 mm with a total magnification of 30X. Figure 6 shows a typical worn image of a coated carbide insert with flank wear (VB_{max}= 0.4 mm).

Wavelet transform for image processing

Mallat first introduced the use of wavelets for the analysis of textures[40]. Discrete wavelet transform (DWT) is an adequate wavelet transform, widely used in image processing for denoising and extracting textural features. However, it has disadvantages like shift variance, lack of directionality, absence of phase information, and aliasing. The slight input signal change creates essential changes in the wavelet coefficient's energy distribution[11]. To overcome these disadvantages, Kingsbury 1998 suggested DTCWT, which estimates the complex transformation of a signal into two distinct DWT decompositions. When the filters used in one tree are intended differently

Specifications of Form Talysurf 50	
Make	Taylor Hobson
Model	Form Talysurf
Speed of traverse	1 mm/s
Gauge range	100 µm
Resolution	0.01 µm
Accuracy	2% of reading
Pickup	Inductive type
Parameters measurable	$R_a/R_z/Rs_m$

Table 4. Specifications of surface roughness measurement device.

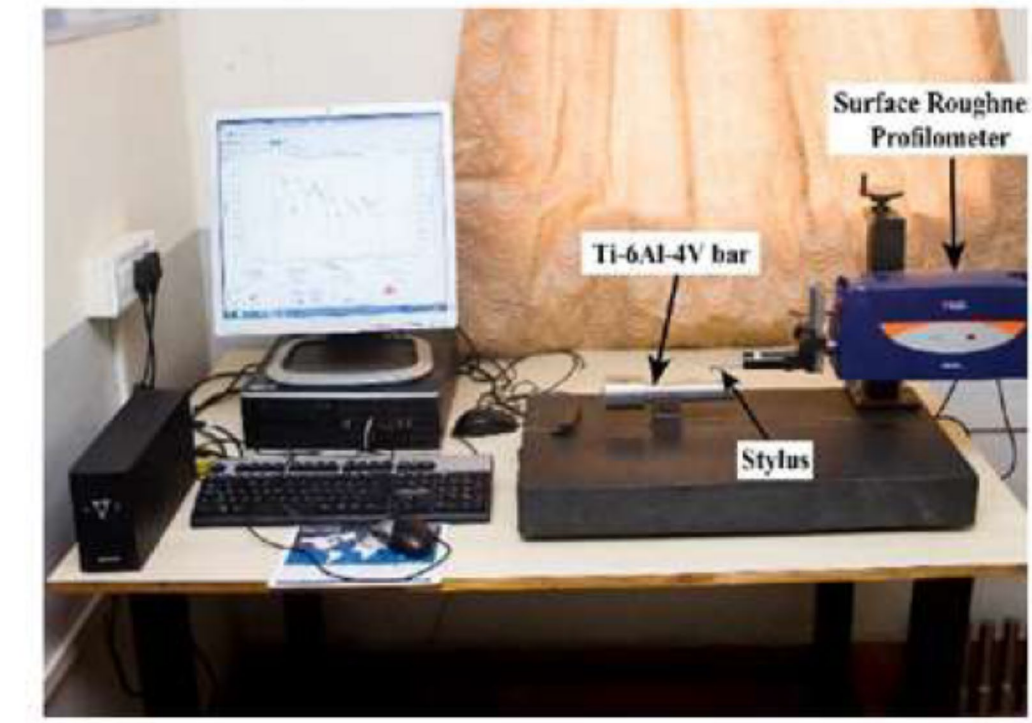

Fig. 5. Surface roughness measurement.

from those used in the other, then it is possible to generate real coefficients for the first DWT, and the second DWT can produce imaginary coefficients. Using Eq. (1), DTCWT applied to an image I(x, y) can be decomposed into 6 complex functions of scaling and 6 complex coefficients of wavelet as mentioned in[41].

$$I(X,Y) = \sum_{l\in Z^2} A_{j_0,l}\emptyset_{j_0,l}(x,y) + \sum_{k\in\alpha}\sum_{j=1}^{j_o}\sum_{l\in Z^2} D^k_{j,l}\varphi^k_{j,l}(x,y) \quad (1)$$

Where j_o is the level of decomposition, $A_{j_0,l}$ and $D^k_{j,l}$represents coefficients of scaling and wavelets, respectively. $\emptyset_{j_0,l}(x,y)$represent the scaling function and $\varphi^k_{j,l}(x,y)$represents 6 wavelet coefficients at angles of $\pm15°$, $\pm45°$, $\pm75°$. Therefore, it produces 6 directionally selective sub-bands for each scale. Thus, DTCWT decomposes the images in 12 directions with 6 real and 6 imaginary coefficients in 2 dimensions[42].

DTCWT image fusion

The input images undergo first-level decomposition using the DTCWT with the bior 2.4 as the mother wavelet. DTCWT image fusion involves decomposing two input images into high-frequency coefficients H_1andH_2, as well as low-frequency coefficients A_1 andA_2. The maximum selection fusion rule is a widely used and effective method for combining high-frequency coefficients in image fusion[43]. The high-frequency coefficients of multi-focus pictures, decomposed using the DTCWT, are fused using the maximum selection fusion rule, as shown below:

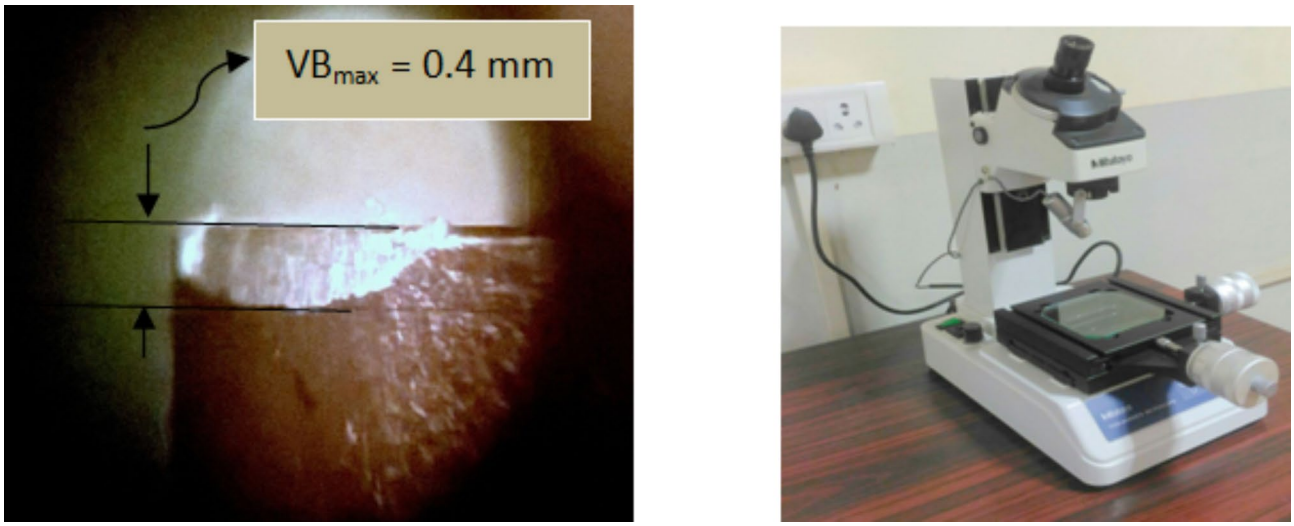

Fig. 6. (**a**) Worn image of coated carbide insert. (**b**) Tool Maker's Microscope.

$$H_F = \begin{cases} H_1, & abs\,(H_1) \geq abs\,(H_2) \\ H_2, & \text{otherwise} \end{cases} \tag{2}$$

The coefficients of low frequency are fused usually using pixel based weighted average fusion rule (PBAVE) which is represented as follows.

$$L_F = W_1 \times A_1 + W_2 \times A_2 \tag{3}$$

Where, W_1 and W_2 are the weights, which take values between 0 and 1 and total sum equal to 1. When set to 1 and 0 individually, Eq. (3) becomes the fusion rule of selection. The weights are usually kept at 0.5. This functions suits well with images from the same modality. When it comes to merging multimodal images with different dynamic ranges, using PBAVE significantly alters the intensity range of the image. It diminishes the contrast of the resulting merged image. These disadvantages can be reduced using region-based image fusion.

DTCWT image fusion technique with PSO

Motivated by birds swarming, PSO was introduced in 2001 by Kennedy and Eberhart[44]. PSO is a well-known bioinspired algorithm used to optimize problems, which essentially involves a machine learning method inspired by swarming birds in search of food loosely[45]. In the context of PSO, the term "particles" is used to represent the number of possible solutions. These particles navigate the search space to optimize the given problem. The subsequent position of a particle is determined by its current velocity and position. The mathematical model of the particle's velocity and position are given by Eqs. (4) and (5) correspondingly.

$$v_{pq}\,(i+1) = w_1.v_{pq}\,(i) + c_1.r_{1q}[y_{pd}\,(i) - x_{pq}\,(i)] + c_2.r_{2q}[\widehat{y}_d\,(i) - x_{pq}\,(i)] \tag{4}$$

$$x_{pq}\,(i+1) = x_{pq}\,(i) + v_{pq}\,(i+1) \tag{5}$$

Here, p represents the p^{th} swarm particle, q gives the q^{th} dimension of particle p. y represents particle p's best location, $\widehat{y}$ is the global best of the entire swarm, i represent a number of iterations, r_1 and r_2 are random numbers between 0 and 1, w_1 is weight, and c_1 and c_2 are learning factors. PSO's main strength is rapid convergence towards the final solution. Consequently, PSO has gained extensive application in optimizing practical issues[45].

The input images undergo decomposition into low-frequency and high-frequency coefficients using DTCWT. A_1 and A_2 represent the coefficients of low frequency in two input images. To emphasize the distinctive characteristics of the source photos, A_1 and A_2 are blended using a region-based approach. The images A_1 and A_2 are segmented using spectral segmentation with multiscale graph decomposition, as described by Timothee et al.[46]. $\{R_1, R_2, \text{ and } R_k\}$ refers to segmentation maps, where R_k represent an individual area. Nevertheless, the related regions are combined using a fusion algorithm based on weighted averages. The weights are dynamically determined using PSO with Piella's index as the fitness function. The low-frequency coefficients are fused in a region-wise manner using a weighted average fusion rule, defined as follows:

$$L_{F,R_k} = w_k \times A_{1,R_k} + (1 - w_k) \times A_{2,R_k} \quad k = 1, 2, \ldots K, \tag{6}$$

L_{F,R_k} represents the fused coefficients of R_k corresponding to A_{1,R_k} and A_{2,R_k}.

The weight values$w_1, w_2 \ldots w_K$, for each region are taken between 0 and 1.

PSO is utilized to determine the ideal contrast setting, denoted dynamically, $w_{o1}, w_{o2}, \ldots, w_{oK}$. Within the context of PSO optimization, a solitary particle serves as a potential solution to the given optimization problem. A solitary particle denotes the weights of K regions. Thus, every individual particle xi is formulated as:

$$X_i = (W_{i,1}, \ldots, W_{i,k}, \ldots, W_{i,K}) \tag{7}$$

$W_{i,k}$ represents the weight of the k^{th} area for the i^{th} particle. The fitness function is employed to evaluate the performance of every individual particle. The fitness function utilized to maximize local contrast in the fused findings is Piella's index Q_W[47]. This index provides a robust measure to ensure the quality of the fusion process and effectively guides the optimization of individual particles' performance. The 8×8 block size determines the amount of salient information (contrast) displayed on the fused image, as seen below:

$$Q_w(I_1, I_2, F) = \sum_{n \in N} c(n)\left(\lambda(n) Q_0(I_1, F/n) + (1 - \lambda(n)) Q_0(I_2, F/n)\right) \tag{8}$$

$$\text{Where } Q_0 = \frac{4\sigma_{xy}\,\bar{x}\bar{y}}{(\bar{x}^2 + \bar{y}^2)(\sigma^2_x + \sigma^2_y)} \tag{9}$$

$$\text{and } \lambda(n) = \frac{s(I_1/n)}{s(I_1/n) + s(I_2/n)} \tag{10}$$

Where, Q_0 is image similarity between two images x and y, described with image statistical features (σ_x, σ_y are variance, σ_{xy} covariance, and mean $\bar{x}$,$\bar{y}$) throughout the images for all blocks (n). In Eq. (8), $Q_0(I_1, F/n)$ is Q_0, which is defined between image I_1 and fused image for local window n.

Q_w is determined by using λ (n) the local saliency weight and Q_0 as given in Eq. (8). $\lambda(n)$ is estimated with $s(I_1/n)$ and $s(I_2/n)$ using Eq. (10). $s(I_1/n)$gives a few saliencies of image I_1 in window n. This study examines the concept of contrast as a measure of saliency to accurately estimate the ideal local contrast in the fused outcomes. The overall saliency of the window is considered as, $c(n) = \max\left[s\left(\frac{I_1}{n}\right), s\left(\frac{I_2}{n}\right)\right]$

As per the formulation of the fitness function in Eq. (8), the most critical aspect is to maximize the value of Q_w. This value represents the significant information included in the input images, successfully preserved in the fused images without distortions. The fused image's optimal local contrast is attained by optimizing the parameterQ_w. Ultimately, the low-frequency coefficients are combined using Eq. (6) with optimized weights$w_{o1}, w_{o2}, \ldots, w_{oK}$. Figure 7 illustrates the proposed fusion rule.

PSO parameters: The acceleration coefficients are defined as =2.5, =1.5. After consulting the literature review[48,49], we conducted a parametric study for PSO parameter optimization. The sensitivity of the PSO parameters (inertia weights, swarm size, and iterations) was studied to tune the parameters that could hit the global convergence. For the fixed swarm size and iteration of 50 and 50, the inertia weight values are optimized by varying between zero and one with 20 different trials. The number of iterations and optimized inertia weight values of 50 and 0.5 were fixed, and the swarm size varied between 20 and 100. The optimized swarm size that

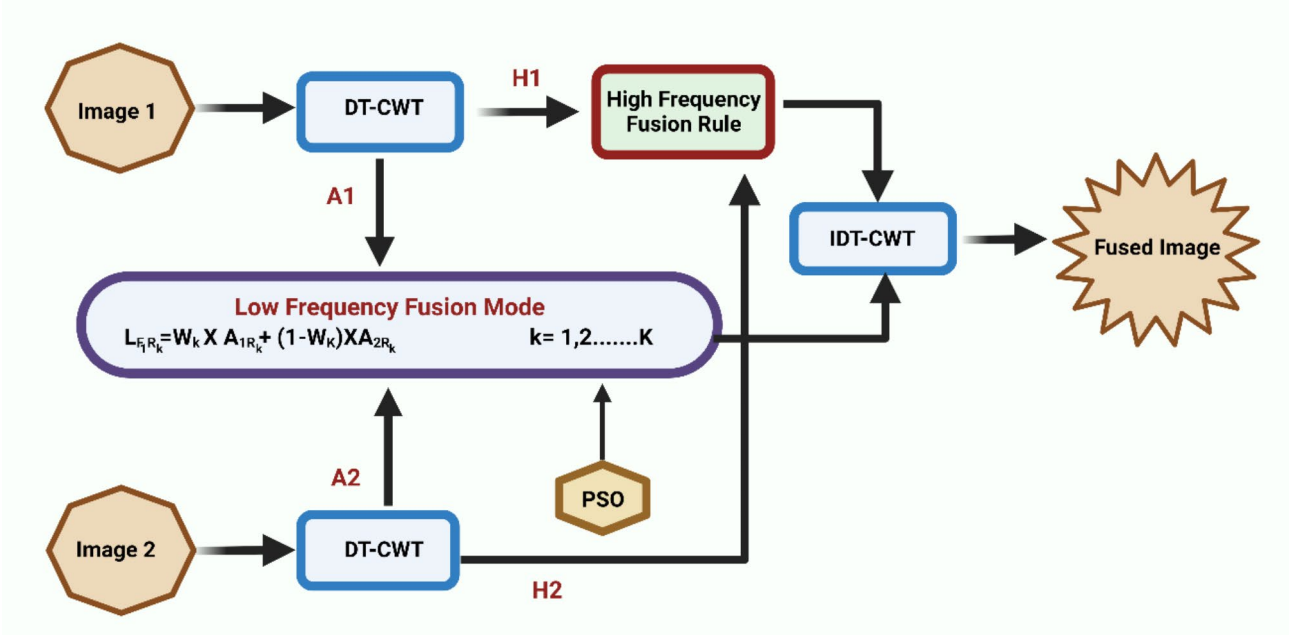

Fig. 7. Diagram of suggested fusion rule[11].

improves fitness value is equal to 30. Finally, iterations are varied between 50 and 100 after maintaining the optimized inertia weight and swarm size. Note the final optimized values that improve the fitness solution with inertia weight, swarm size, and iterations maintained at 0.5, 30, and 40, respectively.

GLCM feature extraction

In 1973, Haralick et al.[50] implemented GLCM, a widely used and well-known texture analysis technique. A GLCM gives an image's joint gray-level histogram in matrix form. The GLCM matrix $\mathrm{Q}(\mathrm{X},\mathrm{Y}|\mathrm{d},\theta)$ includes the statistical features of second order for gray-levels of intensities x and y at a distance d and appropriate angles θ[42].

After applying GLCM, 15 features (F1 to F15) were extracted (see Table 5)[21,51]. The GLCM with distance d= 1 and $\theta = \{0^\circ, 45^\circ, 90^\circ, 135^\circ\}$ have been considered to extract these features[51], which are described in Table 5.

Feature selection using PCA

In 1901, PCA was proposed by Karl Pearson, and later it was evolved as a statistical analysis tool by Hotelling[52]. In image processing, sometimes a greater number of statistical features are extracted than really required. PCA helps in reducing the size of the statistical features. The procedure for PCA implementation is explained as follows[53].

In 1901, Karl Pearson proposed PCA, which later evolved as a statistical analysis tool by Hotelling[52]. In image processing, sometimes a greater number of statistical features are extracted than really required. PCA helps reduce the size of the statistical features. The procedure for PCA implementation is explained below[53].

1. Consider the entire extracted feature in matrix form

   $\mathrm{R_{p,q}}, \mathrm{p} = (1,2,\ldots,\mathrm{m})$, m represents the number of experiments considered; $\mathrm{q} = (1,2,\ldots,\mathrm{n})$, n gives extracted number of features.
   For this work m=number of experiments, n=number of extracted features

$$X = \begin{bmatrix} y_1(1) & y_1(2) & \ldots & y_1(n) \\ y_2(1) & y_2(2) & \ldots & y_2(n) \\ . & . & \ldots & . \\ . & . & \ldots & . \\ y_m(1) & y_m(2) & \ldots & y_m(n) \end{bmatrix} \tag{11}$$

Feature Name	Equation
Autocorrelation	$\mathrm{F1} = \sum_{\mathrm{y}=0}^{\mathrm{K}-1}\sum_{\mathrm{z}=0}^{\mathrm{K}-1}(\mathrm{yz})\,\mathrm{X}(\mathrm{y},\mathrm{z})$
Contrast	$\mathrm{F2} = \sum_{\mathrm{y}=0}^{\mathrm{K}-1}\mathrm{n}^2\left\{\sum_{\mathrm{y}=1}^{\mathrm{K}}\sum_{\mathrm{z}=1}^{\mathrm{K}}\mathrm{X}(\mathrm{y},\mathrm{z})\right\},\ \lvert\mathrm{y}-\mathrm{z}\rvert = \mathrm{n}$
Correlation	$\mathrm{F3} = \frac{\sum_{\mathrm{y}}\sum_{\mathrm{z}}(\mathrm{yz})\mathrm{X}(\mathrm{y},\mathrm{z}) - \mu_{\mathrm{y}}\mu_{\mathrm{z}}}{\sigma_{\mathrm{y}}\sigma_{\mathrm{z}}}$
Cluster prominence	$\mathrm{F4} = \sum_{\mathrm{y}=0}^{\mathrm{K}-1}\sum_{\mathrm{z}=0}^{\mathrm{K}-1}\{\mathrm{y}+\mathrm{z}-\mu_{\mathrm{y}}-\mu_{\mathrm{z}}\}^4\mathrm{X}_{(\mathrm{y}+\mathrm{z})}$
Dissimilarity	$\mathrm{F5} = \sum_{\mathrm{y}=0}^{\mathrm{K}-1}\sum_{\mathrm{z}=0}^{\mathrm{K}-1}\lvert\mathrm{y}-\mathrm{z}\rvert\,\mathrm{X}(\mathrm{y},\mathrm{z})$
Energy or uniformity	$\mathrm{F6} = \sum_{\mathrm{y}=0}^{\mathrm{K}-1}\sum_{\mathrm{z}=0}^{\mathrm{K}-1}\{\mathrm{X}(\mathrm{y},\mathrm{z})\}^2$
Entropy	$\mathrm{F7} = -\sum_{\mathrm{y}=0}^{\mathrm{K}-1}\sum_{\mathrm{z}=0}^{\mathrm{K}-1}\mathrm{X}(\mathrm{y},\mathrm{z})\log(\mathrm{X}(\mathrm{y},\mathrm{z}))$
Homogeneity	$\mathrm{F8} = \sum_{\mathrm{y}=0}^{\mathrm{K}-1}\sum_{\mathrm{z}=0}^{\mathrm{K}-1}\frac{\mathrm{X}(\mathrm{y},\mathrm{z})}{1+\lvert\mathrm{y}-\mathrm{z}\rvert}$
Maximum probability	$\mathrm{F9} = Max_{y,z}\mathrm{X}(\mathrm{y},\mathrm{z})$
Sum of squares	$\mathrm{F10} = \sum_{\mathrm{y}=0}^{\mathrm{K}-1}\sum_{\mathrm{z}=0}^{\mathrm{K}-1}(\mathrm{y}-\mu_{\mathrm{y}})^2\mathrm{X}(\mathrm{y},\mathrm{z})$
Sum average	$\mathrm{F11} = \sum_{\mathrm{y}=0}^{2\mathrm{K}-2}\mathrm{y}\mathrm{X}_{(\mathrm{y}-\mathrm{z})}(\mathrm{y})$
Sum variance	$\mathrm{F12} = \sum_{\mathrm{y}=2}^{2\mathrm{K}}(\mathrm{y}-\mathrm{f_s})^2\mathrm{X}_{\mathrm{y}+\mathrm{z}}(\mathrm{y})$
Sum entropy	$\mathrm{F13} = \sum_{\mathrm{y}=2}^{2\mathrm{K}}\mathrm{X}_{(\mathrm{y}+\mathrm{z})}(\mathrm{y})\log\{\mathrm{X}_{(\mathrm{y}+\mathrm{z})}(\mathrm{y})\}$
Difference variance	$\mathrm{F14} = \mathrm{Varianceof}\mathrm{X}_{(\mathrm{y}-\mathrm{z})}$
Difference entropy	$\mathrm{F15} = -\sum_{\mathrm{y}=0}^{\mathrm{K}-1}\mathrm{X}_{(\mathrm{y}-\mathrm{z})}(\mathrm{y})\log\{\mathrm{X}_{(\mathrm{y}-\mathrm{z})}(\mathrm{y})\}$

Table 5. GLCM features extracted[15,34]. where, K gives the gray level values used in $\mathrm{X}(\mathrm{Y},\mathrm{Z})$, μ = mean value of $\mathrm{X}(\mathrm{Y},\mathrm{Z})$, and $\mathrm{X}(\mathrm{Y},\mathrm{Z})$denotes the GLCM element, one having intensity y another having intensity z.

2. By using Eq. (12), the covariance coefficient is calculated for statistical features of the second order.

$$R_{p,q} = \left[\frac{\mathrm{Cov}(C_i(p), C_i(q))}{\sigma C_i(p)\,\sigma C_i(q)}\right] \tag{12}$$

where, $\mathrm{Cov}C_i(p)$, $\mathrm{Cov}C_i(q)$ is the covariance of sequences $C_i(p)$, $C_i(q)$; $\sigma C_i(p)$, and $\sigma C_i(q)$, are the standard deviation of sequences $C_i(p)$ and $C_i(q)$ respectively.

3. The Eigen values and Eigen vectors are calculated using covariance coefficients

$$(R - \lambda_k I_m)\, V_{ik} = 0 \tag{13}$$

Where λ_k is eigen values,

$$\sum_{k=1}^{n} \lambda_k = n, \quad k = 1,2 \ldots n, \tag{14}$$

and $V_{ik}[a_{k1}, a_{k2}, \ldots., a_{km}]^T$ are eigen vectors corresponding to λ_k

4. Uncorrelated principal components are determined using

$$P_{mk} = \sum_{i=1}^{n} R_m(i).V_{ik} \tag{15}$$

Where, $P_{m1}$and P_{m2}, are called first principal and second principal component respectively.

ANN based modeling and prediction

Artificial neural networks are extensive used across various domains of application. ANN, short for Artificial Neural Network, is a computational model that emulates human cognition and neurobiology. MLPs, or multi-layer perceptrons can solve challenging and intricate issues using a widely used supervised training approach called back-propagation[23–25]. In addition to MLPNN, the RBFNN is another commonly used ANN model for enhancing approximation. The RBFNN possesses a remarkable capacity to calculate non-linear connections between input and output variables. Additionally, the training process of RBFNN is faster than that of a multi-layer perceptron. It has a simpler network structure, uses faster learning algorithms, and has local tuning and better approximation capabilities[26,27]. Due to all these advantages, RBFNN has been commonly found in various scientific and engineering applications.

RBFNN

The RBFNN network comprises three layers: an input layer, a hidden layer consisting of neurons with Gaussian activation functions, and an output layer with nonlinear activation functions. The RBFNN consists of a single hidden layer. The system does a complex, nonlinear conversion from the input to the hidden layer. RBF units have two key variables, namely the center and its width or deviation, represented by μ_i and σ_j respectively[26]. The hidden layer of neurons, described by Eq. (16), employs Gaussian transfer functions.

$$\varphi_i(\mu) = -\left(\frac{\|x - \mu_i\|^2}{2\sigma_j^2}\right) \tag{16}$$

Let x represent the input variable, μ_i represent the center variable of the RBF unit, and σ_j represent the variance of the Gaussian function or the breadth of the RBF unit. Equation (17) determines the output of the output layer.

$$Y = \frac{1}{1 + e^{-\sum w_i \varphi + b}} \tag{17}$$

φ represents the activation function of the radial basis units. The weights w_i determine the multiplication factor for the output of a radial basis function (RBF) unit in the output layer, whereas b represents a bias[54]. The RBFNN employs the Conditional Fuzzy C-Means (CFC-M) method to determine the number of units and the placement of their centers in the RBF units.

RBFNN models	Details
Model 1	DTCWT and GLCM image processing method (15 features).
Model 2	DTCWT and GLCM image processing method (10 PCA selected features).
Model 3	DTCWT image fusion and GLCM image processing method (15 features).
Model 4	DTCWT image fusion and GLCM image processing method (10 PCA selected features).
Model 5	DTCWT image fusion with PSO and GLCM image processing method (15 features).
Model 6	DTCWT image fusion with PSO and GLCM image processing method (10 PCA selected features).

Table 6. RBFNN models.

Sl no.	Performance metric	DTCWT method	DTCWT image fusion method	DTCWT image fusion with PSO method
1	PSNR	26.9423	26.9441	43.3082
	RMSE	0.0155	0.0155	0.0025
2	PSNR	22.6628	28.5809	42.0238
	RMSE	0.0164	0.0113	0.0019
3	PSNR	21.8979	21.9115	33.4397
	RMSE	0.0194	0.0194	0.0085

Table 7. PSNR and RMSE for sample images of turned surfaces.

RBFNN model development

RBF neural networks have been employed to model and forecast the surface roughness of rotated surface pictures. For the current work, 6 RBFNN models have been developed. For RBFNN models 1, 3, and 5, the extracted 15 GLCM features from each image processing method, cutting speed, feed rate, depth of cut and tool flank wear are given as inputs. For RBFNN models 2, 4, and 6, PCA selected features (10 features) from each image processing method and other variables as before are considered inputs. Table 6 shows details of RBFNN models.

Result and discussions

The proposed DTCWT image fusion with the PSO, image processing method is used to estimate the surface roughness of Ti-6Al-4 V turned surfaces. The proposed image processing method is compared with DTCWT image fusion without PSO and with DTCWT (without image fusion). Peak Signal to Noise Ratio (PSNR) and Root Mean Square Error (RMSE) are calculated to compare the performance of different image processing methods. Further comparisons of these methods have been done using RBFNN models. Due to minor changes in lighting during image acquisition, the machined surface photographs show non-uniform illumination; the assessment length is 12.5 mm. Therefore, image pre-processing is necessary to ensure consistent brightness in all photos of machined surfaces. Image pre-processing involves image cropping, gray-scale conversion, etc. All the captured images were cropped to 256×256 pixel resolution using Picasa software before using it for image processing. The digital image is transformed into a gray-scale, as each pixel's value represents a single sample, conveying intensity information in the resulting gray-image. The image is composed of a range of gray tones, from the darkest black to the brightest white. The performance evaluation of three image processing methods and model performance are given in the following sections.

Performance evaluation in terms of PSNR and RMSE

Different objective performance evaluation measures have been used to determine the quality of the processed images, out of which PSNR and RMSE is essential. PSNR represents the relationship between the processed image and the original image. A Higher PSNR value means better quality of the image[18]. The RMSE metric assesses the image's quality by comparing the original and processed images. A higher RMSE value indicates a more significant variance between the original and processed images.

The equation for PSNR is

$$\mathrm{PSNR} = 10\log\frac{255^2}{\mathrm{RMSE}^2} \tag{18}$$

where the RMSE is defined using equation

$$\mathrm{RMSE} = \frac{1}{\mathrm{MN}}\sum_{\mathrm{l}=1}^{\mathrm{M}}\sum_{\mathrm{k}=1}^{\mathrm{N}}[\mathrm{R}(\mathrm{l},\mathrm{k}) - \mathrm{F}(\mathrm{l},\mathrm{k})]^2 \tag{19}$$

Where $\mathrm{F}(\mathrm{l},\mathrm{k})$ is the processed image, $\mathrm{R}(\mathrm{l},\mathrm{k})$ is the original image, and M × N is the size of the images. Table 7 shows the PSNR and RMSE values for a sample of turned image surfaces for three image processing methods.

The proposed DTCWT image fusion with the PSO method has resulted in the highest PSNR values with the lowest RMSE. These findings demonstrate that the suggested image processing technique yields photos of superior quality.

Performance of RBFNN model 1

GLCM is directly related to image intensity, which may consider information about patterns of mutual occurrence. For one set of data, three images are captured; accordingly, the average of three statistical features is considered for modelling. Table 8 shows a sample of extracted features for cutting speed 150 m/min, feed rate 0.20 mm/rev, and depth of cut 0.8 mm.

The RBFNN training process is an iterative method in which the entire training data set is repeatedly given to the RBF neural network untill the Mean Square Error (MSE) value converges to a set value. Based on similar work[26], an MSE value of 0.001 has been considered for determining the prediction accuracy of developed models. In this work, the MSE is calculated using Eq. (20).

$$\mathrm{MSE} = \frac{1}{\mathrm{n}} \sum_{\mathrm{i}=1}^{\mathrm{n}} \left(\mathrm{X_i} - \widetilde{\mathrm{X}}_{\mathrm{i}} \right)^2 \tag{20}$$

Let $\mathrm{X_i}$ represent the $\mathrm{i^{th}}$ element of the actual values and $\widetilde{X}_i$ represent the $\mathrm{i^{th}}$ element of the predicted values. n represents the total number of data points.

RBFNN uses CFCM to fix the number of units and the center location in the RBF units. The training of CFCM was performed with different centers, and the target error was set at 0.001. The width parameter controls the refining properties of the interpolating function[26]. The widths have been kept constant and are selected by trial and error to minimize the MSE and maximize the prediction accuracy obtained. The training has been carried out for width values of 0.15, 0.20, and 0.25. The network has been trained by varying the RBF units between 20 and 50. The model with RBF unit's results in maximum prediction accuracy and minimum MSE is considered. The simulation parameters remained constant, specifically with a learning rate of 0.85, a momentum rate of 0.05, and a maximum number of epochs set at 1000. The model with RBF units results in maximum prediction accuracy, and minimum MSE is considered. Table 9 shows the obtained results for RBFNN model 1 for 20 RBF units. It is observed that the prediction accuracy is maximum with minimum MSE for width 0.15. However, with a further increase in width, the performance of Model 1 decreases with an increase in MSE. However, with a further increase in width, the performance of Model 1 decreases with an increase in MSE.

Table 10 gives the input parameters for surface roughness prediction for RBFNN model 1 (speed rate, feed rate, depth of cut, tool flank wear, and 15 GLCM features). It compares surface roughness for 27 experiments measured using the direct and image processing methods, along with errors obtained. Each experiment consisted of several machining passes (each of 48 mm). This table considers a randomly selected $\mathrm{R_a}$ value from each machining experiment. The percentage error for the RBFNN model was estimated using Eq. (21), which gives the relative error.

$$\mathrm{R_e} = \left| \left(\frac{\mathbf{V_m} - \mathbf{V_p}}{\mathbf{V_m}} \right) \right| \times 100 \tag{21}$$

Where $\mathrm{R_e}$ gives relative accuracy of the model, $\mathbf{V_m}$ is value of stylus measured and $\mathbf{V_p}$ gives the value predicted.

In predictive modeling, especially when dealing with high-dimensional data, PCA can help reduce the number of features while retaining the most important information. PCA selects the Eigenvectors with large Eigenvalues from higher to lower significance, eliminating the features with lower significance. Table 11 shows the Eigenvalues and proportion of principal components. Ten features were selected out of 15 GLCM features, and the Autocorrelation feature is the most dominant because of its highest contribution percentage of 60.72%. Parameters with a higher percentage contribution are ranked higher regarding the significance of textural characteristics.

The inputs for RBFNN model 2 consist of PCA-selected features, including autocorrelation, contrast, correlation, cluster prominence, dissimilarity, energy or uniformity, entropy, homogeneity, maximum probability, and sum of squares. These features are combined with machining parameters and tool flank wear. The outcomes acquired for the second RBFNN model are displayed in Table 12. An increase in prediction accuracy of 0.28% is seen for the training data and 1.08% for the test data when using 25 RBF units with a width of 0.15.

Performance of RBFNN model 3 and model 4

The RBFNN models 3 and 4 utilize DTCWT image fusion with GLCM characteristics. An iterative process of experimentation sets the breadth of the RBF units. The network attains optimal prediction accuracy utilizing 25 RBF units during training. For RBFNN model 3, from Table 12, it is observed that for 25 RBF units and 0.15 width, the prediction accuracy is maximum, and MSE is minimum. Expanding the width further leads to a decline in network performance and an increase in MSE. The RBFNN model 4 achieves the highest performance with a width of 0.15, with prediction accuracies of 98.91% for training data and 98.84% for test data, along with a minimal MSE of 0.0144.

Performance of RBFNN model 5 and model 6

RBFNN models 5 and 6 are based on DTCWT image fusion with PSO for GLCM-based image processing. The RBFNN model 5 achieves the highest prediction accuracy for training and test data, with the lowest MSE, using a width of 0.15 and 35 RBF units. The training data has a prediction accuracy of 98.84%, and the test data

Sl. no.	F1	F 2	F 3	F 4	F 5	F 6	F 7	F 8	F 9	F 10	F 11	F 12	F 13	F 14	F 15
1	53.6270	0.3829	0.4517	3.0551	0.3668	0.2445	1.6362	0.8191	0.3838	53.6201	14.6245	177.1753	1.3520	0.3829	0.6889
2	56.1399	0.2976	0.6102	6.2437	0.2898	0.2734	1.5444	0.8564	0.4172	56.1032	14.9542	186.9599	1.3259	0.2976	0.6191
3	53.2188	0.3865	0.3941	2.6610	0.3737	0.2645	1.5828	0.8153	0.4264	53.1962	14.5730	177.1381	1.2971	0.3865	0.6893
4	55.2169	0.3388	0.6009	6.7130	0.3283	0.2421	1.6584	0.8376	0.3687	55.2013	14.8273	181.4230	1.4085	0.3388	0.6558
5	52.5544	0.4248	0.3360	2.8322	0.3938	0.2775	1.5937	0.8079	0.4555	52.5540	14.4840	175.1888	1.2805	0.4248	0.7248
6	54.5413	0.4063	0.3483	2.5797	0.3894	0.2510	1.5592	0.8080	0.3674	54.5113	14.7557	182.9728	1.2601	0.4063	0.7032
7	53.5953	0.4148	0.3364	2.4695	0.3958	0.2599	1.5768	0.8052	0.4098	53.5686	14.6274	179.2697	1.2695	0.4148	0.7106
8	52.6207	0.4294	0.3239	3.4363	0.3918	0.2877	1.5619	0.8096	0.4661	52.6136	14.4938	176.0782	1.2561	0.4294	0.7248

Table 8. Sample of extracted features for speed 150 m/min, feed rate 0.20 mm/rev, and 0.8 mm depth of cut.

Width	0.15	0.20	0.25
Training data accuracy (%)	97.3988	92.3913	79.7688
Test data accuracy (%)	95.6522	90.9075	73.9130
Average MSE	0.0179	0.0313	0.0742

Table 9. Performance of RBFNN model 1 for 20 RBF units.

has a prediction accuracy of 97.82%, with a MSE of 0.0148. Table 12 shows an additional improvement in the prediction accuracy of the RBFNN model 6. The results indicate that the highest prediction accuracy and lowest MSE are achieved by using 35 RBF units with a width of 0.15. The highest achieved prediction accuracy is 100% for the training data and 99.13% for the test data, with a minimum MSE of 0.0131.

Comparative performance analysis of RBFNN models

The suggested image processing technique has been compared with two other methods and 6 RBFNN models have been built for surface roughness modeling and prediction of turned surface images. Table 13 gives a comparative evaluation of the performance of developed RBFNN models for evaluating the different image processing methods. The prediction accuracy obtained for model 2 is slightly higher than that of model 1. Model 2 utilizes PCA to choose GLCM characteristics as inputs for the RBFNN model. This process eliminates irrelevant information and enhances the accuracy of predictions. In the image fusion approach, the high-frequency coefficients are combined using the maximum selection fusion rule, while the low-frequency coefficients are mixed using the pixel-based weighted average fusion rule. The main reason for using multi-focus image fusion method is to gather all the required information from the original images, generate no additive noise, and prevent edge textures with high contrast[55]. Enhancing the quality of retrieved GLCM features results in a 1.51% increase in prediction accuracy for the training data and a 2.9% increase for the test data in RBFNN model 3. For RBFNN model 4, a prediction accuracy of 1.51% can be observed for training data, with a 3.19% improvement in prediction accuracy for test data. Many pixels-based multi-focus image fusion methods have low spatial resolution and blurring effects[55]. The adoption of region-based image fusion helps to mitigate these constraints. Region-based image fusion uses PSO to compute the ideal contrast setting automatically, resulting in an optimal fused image. Enhancing the quality of the merged image subsequently enhances the performance of RBFNN model 6.

The RBFNN model 6 gives 100% accuracy for training data and 99.13% for test data with a least MSE of 0.0131, which is the highest compared to the remaining RBFNN models. This model is based on features extracted using DTCWT image fusion with PSO. Thus, RBFNN quantitatively establishes the superiority of this image-processing method. It is also observed that DTCWT image fusion results are good compared to DTCWT without fusion. Figure 8 compares surface roughness in terms of stylus measured actual R_a and predicted R_a using RBFNN model 6 for randomly selected test data ranging from a minimum of 0.3910 to a maximum of 1.3852 µm. The results indicate a high level of forecast accuracy and consistent measurements, as all repeated measurements revealed a difference of less than 4.0%. The projected R_a values closely match the experimental readings. Therefore, there is a strong correlation between the measured and projected R_a values. However, RBFNN model 6 uses a maximum number of 35 RBF units, making the ANN model less compact.

Validation test

RBFNN model 6, which gives better prediction results, is considered for validation. For validation purposes, out of 461 data sets, 23 data sets that were neither used in training nor test sets were considered for analysis. It is noticed that, there has been a good agreement between both the actual measured R_a and predicted $R_a$with a minimum error of 1.44% and a 2.48% average prediction error for randomly selected data. Hence, the developed image processing method using DTCWT image fusion with PSO can be effectively used for better modeling and surface roughness prediction from turned surface images using GLCM-based features and selecting the most sensitive features using PCA. Table 14 gives the error obtained for randomly selected data.

Further, to validate the developed model and the outcome of this work, a set of shaping operations was carried out on a conventional shaping machine under different cutting conditions. Mild steel specimens have been used for machining operations. The computer vision system has successfully captured images of the surfaces. The best quality of shaped surface images was obtained at approximately 15 cm distance. For this study, 18 images of shaped surfaces were considered. The surface roughness values for shaped surfaces vary from a minimum of 4.0168 to a maximum of 7.5991 µm. The GLCM features have been extracted from the shaped images using the approach described in this paper. The extracted GLCM features have been treated as validation data to check the generalization capability of RBFNN model 6. For this experimental data, the maximum prediction accuracy for training and test data with minimum MSE is obtained for 0.15 width and 25 RBF units. The prediction accuracy for training data is 100%, and 97.12% is for test data, with a minimum MSE of 0.017, as shown in Table 15.

Based on the information presented in Table 16, the errors observed in the selected, shaped image data were analysed. It was found that the $R_a$values measured by the stylus were very similar to the predicted values. This suggests a correlation between the experimental and the predicted R_a values validating the effectiveness of our proposed method (RBFNN model 6), in modelling and predicting the surface roughness of Ti-6Al-4 V turned images.

Exp. no.	Speed	Feed	DOC	Flank Wear	F1	F 2	F 3	F 4	F 5	F 6	F 7	F 8	F 9	F 10	F 11	F 12	F 13	F 14	F 15	Direct method R_a	Image processing R_a	Error (%)
1	150	0.15	0.8	0.080	62.2207	0.0644	0.6932	0.8938	0.0606	0.7399	0.5614	0.9703	0.8549	62.0018	15.7668	233.0211	0.5134	0.0644	0.2316	0.8337	0.8217	1.44
2	150	0.20	0.8	0.120	61.3676	0.0301	0.9263	6.5926	0.0284	0.7165	0.6190	0.9861	0.8383	61.1361	15.6433	227.2036	0.5962	0.0301	0.1299	1.3688	1.3513	1.28
3	150	0.25	0.8	0.100	60.9544	0.0191	0.9658	13.3247	0.0176	0.7120	0.6293	0.9914	0.8359	60.6862	15.5801	225.0503	0.6150	0.0191	0.0888	1.2584	1.2459	0.99
4	175	0.15	0.8	0.095	61.2359	0.0122	0.9734	9.5143	0.0120	0.7234	0.5781	0.9941	0.8416	60.9789	15.6220	227.4894	0.5694	0.0122	0.0650	0.5510	0.5610	1.81
5	175	0.20	0.8	0.115	61.0546	0.0206	0.9584	8.3575	0.0199	0.7140	0.6151	0.9901	0.8368	60.8011	15.5972	225.8803	0.6001	0.0206	0.0982	0.7025	0.6860	2.35
6	175	0.25	0.8	0.085	58.7128	0.1153	0.7964	4.2786	0.1143	0.4544	1.0866	0.9430	0.6234	58.5031	15.2954	205.2547	1.0042	0.1153	0.3577	0.9282	0.9062	2.37
7	200	0.15	0.8	0.130	61.3803	0.0240	0.9341	4.4595	0.0225	0.7107	0.5953	0.9890	0.8325	61.1361	15.6474	227.8241	0.5769	0.0240	0.1080	0.4703	0.4863	3.40
8	200	0.20	0.8	0.135	61.6126	0.0217	0.9316	3.4715	0.0215	0.7270	0.5567	0.9893	0.8428	61.3461	15.6799	229.7803	0.5416	0.0217	0.1042	1.3688	1.3368	2.34
9	200	0.25	0.8	0.090	61.3160	0.0148	0.9643	6.4149	0.0131	0.7253	0.5650	0.9937	0.8423	61.0657	15.6354	228.2919	0.5530	0.0148	0.0694	0.8172	0.8317	1.77
10	150	0.15	1.0	0.095	61.2878	0.0136	0.9690	7.5179	0.0132	0.7256	0.5746	0.9935	0.8433	61.0296	15.6302	227.8257	0.5649	0.0136	0.0704	0.6332	0.6201	2.07
11	150	0.20	1.0	0.075	60.7035	0.0457	0.9188	11.9257	0.0457	0.6615	0.7589	0.9771	0.8040	60.4605	15.5493	220.7697	0.7273	0.0457	0.1857	0.6407	0.6216	2.98
12	150	0.25	1.0	0.106	61.5523	0.0264	0.9295	5.7243	0.0264	0.7336	0.5838	0.9868	0.8494	61.3035	15.6688	228.8281	0.5657	0.0264	0.1221	0.6815	0.6670	2.13
13	175	0.15	1.0	0.120	60.9303	0.0232	0.9588	12.0950	0.0231	0.7130	0.6389	0.9884	0.8371	60.6723	15.5770	224.7128	0.6234	0.0232	0.1102	0.6455	0.6305	2.32
14	175	0.20	1.0	0.085	60.5119	0.0521	0.8844	4.8297	0.0520	0.6143	0.7866	0.9740	0.7650	60.2667	15.5323	219.3455	0.7506	0.0521	0.2046	0.5958	0.5857	1.70
15	175	0.25	1.0	0.085	61.2179	0.0144	0.9681	8.5993	0.0139	0.7199	0.5859	0.9932	0.8393	60.9571	15.6204	227.2433	0.5753	0.0144	0.0732	0.7572	0.7381	2.52
16	200	0.15	1.0	0.100	59.0152	0.1258	0.7896	6.0400	0.1235	0.4693	1.1000	0.9386	0.6488	58.8211	15.3335	206.2643	1.0089	0.1258	0.3780	0.3910	0.3809	2.58
17	200	0.20	1.0	0.090	61.3525	0.0387	0.8980	4.3292	0.0372	0.7060	0.6398	0.9817	0.8313	61.0935	15.6438	226.7144	0.6107	0.0387	0.1600	0.6224	0.6186	0.61
18	200	0.25	1.0	0.115	60.1439	0.0472	0.9166	8.9125	0.0467	0.6066	0.8248	0.9767	0.7607	59.9044	15.4770	216.7641	0.7910	0.0472	0.1896	0.7172	0.6982	2.65
19	150	0.15	1.2	0.110	60.7828	0.1147	0.6783	1.7692	0.1139	0.5738	0.8667	0.9432	0.7396	60.6078	15.5772	219.3943	0.7854	0.1147	0.3563	0.5109	0.5235	2.47
20	150	0.20	1.2	0.110	60.7310	0.0251	0.9608	14.0105	0.0221	0.7090	0.6554	0.9894	0.8355	60.4746	15.5466	223.5878	0.6357	0.0251	0.1058	0.6822	0.6973	2.21
21	150	0.25	1.2	0.110	61.6709	0.0744	0.7551	2.7028	0.0728	0.6920	0.6839	0.9639	0.8246	61.4619	15.6916	227.3734	0.6303	0.0744	0.2631	0.7491	0.7281	2.80
22	175	0.15	1.2	0.115	59.4615	0.1374	0.6814	1.2973	0.1371	0.4652	1.0132	0.9315	0.6372	59.2769	15.4032	210.5579	0.9176	0.1374	0.4003	0.4307	0.4509	4.69
23	175	0.20	1.2	0.150	59.6530	0.1500	0.6700	2.1184	0.1475	0.4798	1.0435	0.9266	0.6585	59.4699	15.4273	210.7338	0.9368	0.1500	0.4233	1.1371	1.0996	3.30
24	175	0.25	1.2	0.110	60.4652	0.0283	0.9615	18.7142	0.0259	0.6952	0.7019	0.9874	0.8274	60.2151	15.5063	221.2560	0.6802	0.0283	0.1207	0.9007	0.8677	3.66
25	200	0.15	1.2	0.080	62.7618	0.0273	0.8235	0.8415	0.0232	0.8304	0.3767	0.9890	0.9085	62.5077	15.8365	239.9516	0.3552	0.0273	0.1095	0.5133	0.4962	3.33
26	200	0.20	1.2	0.115	60.6591	0.0206	0.9691	18.0500	0.0204	0.6988	0.6747	0.9898	0.8287	60.4002	15.5353	222.5755	0.6604	0.0206	0.0999	1.3305	1.2985	2.41
27	200	0.25	1.2	0.115	61.2520	0.0146	0.9653	5.9800	0.0143	0.7191	0.5781	0.9929	0.8384	60.9991	15.6269	227.6032	0.5677	0.0146	0.0752	1.3852	1.3342	3.68

Table 10. Input parameters considered for RBFNN model 1 (speed rate, feed rate, depth of cut, tool flank wear, and 15 GLCM features) for surface roughness prediction and comparison of R_a for stylus measured and predicted values along with errors obtained (randomly selected data).

Principal component	Eigen values	Variance (%)
Autocorrelation	9.1090	60.7264
Contrast	3.7143	24.7621
Correlation	1.5485	10.3236
Cluster prominence	0.4368	2.9118
Dissimilarity	0.1194	0.7961
Energy or uniformity	0.0296	0.1971
Entropy	0.0193	0.1286
Homogeneity	0.0116	0.0770
Maximum probability	0.0065	0.0431
Sum of squares	0.0025	0.0165
Sum average	0.0012	0.0082
Sum variance	0.0010	0.0065
Sum entropy	0.0004	0.0026
Difference variance	0.0001	0.0004
Difference entropy	0	0

Table 11. Eigen values and its principal component contributions.

RBFNN model type	Width	Training data accuracy (%)	Test data accuracy (%)	Average MSE
RBFNN model 2 for 25 RBF units	0.15	97.6879	96.7391	0.0162
	0.20	97.3988	95.6522	0.0163
	0.25	97.6879	95.6522	0.0164
RBFNN model 3 for 25 RBF units	0.15	98.9130	98.5549	0.0108
	0.20	98.5549	97.8261	0.0161
	0.25	97.8261	96.5318	0.0420
RBFNN model 4 for 30 RBF units	0.15	98.9130	98.8439	0.0144
	0.20	98.8439	96.7391	0.0222
	0.25	96.7391	94.5087	0.0419
RBFNN model 5 for 35 RBF units	0.15	98.8439	97.8261	0.0148
	0.20	98.2659	94.5652	0.0161
	0.25	97.6879	95.6522	0.0186
RBFNN model 6 for 35 RBF units	0.15	100.0000	99.1329	0.0131
	0.20	100.0000	98.8439	0.0168
	0.25	99.1329	98.9130	0.0173

Table 12. Performance of RBFNN models 2–6.

Model considered	Training data accuracy (%)	Test data accuracy (%)	MSE	No. of hidden neurons
RBFNN model 1	97.3988	95.6522	0.0179	20
RBFNN model 2	98.9130	98.5549	0.0161	25
RBFNN model 3	97.6879	96.7391	0.0164	25
RBFNN model 4	98.9130	98.8439	0.0144	30
RBFNN model 5	98.8439	97.8261	0.0148	35
RBFNN model 6	100	99.1329	0.0131	35

Table 13. Comparative evaluation of developed RBFNN models.

Conclusions

The main objective of this study is to utilize wavelet-based image processing to model and forecast the surface roughness of turned surface images of Ti-6Al-4 V. Three methods of wavelet-based image processing techniques are analyzed: DTCWT, DTCWT Image fusion, and DTCWT image fusion using PSO. From all 3 methods, GLCM-based features were extracted. PCA removes insignificant GLCM extracted features by transforming the correlated responses into uncorrelated responses called principal components. RBFNN models were created by incorporating GLCM features machining parameters and tool flank wear as input variables. The features selected by PCA have been used. Six RBFNN models have been developed and compared regarding prediction accuracy

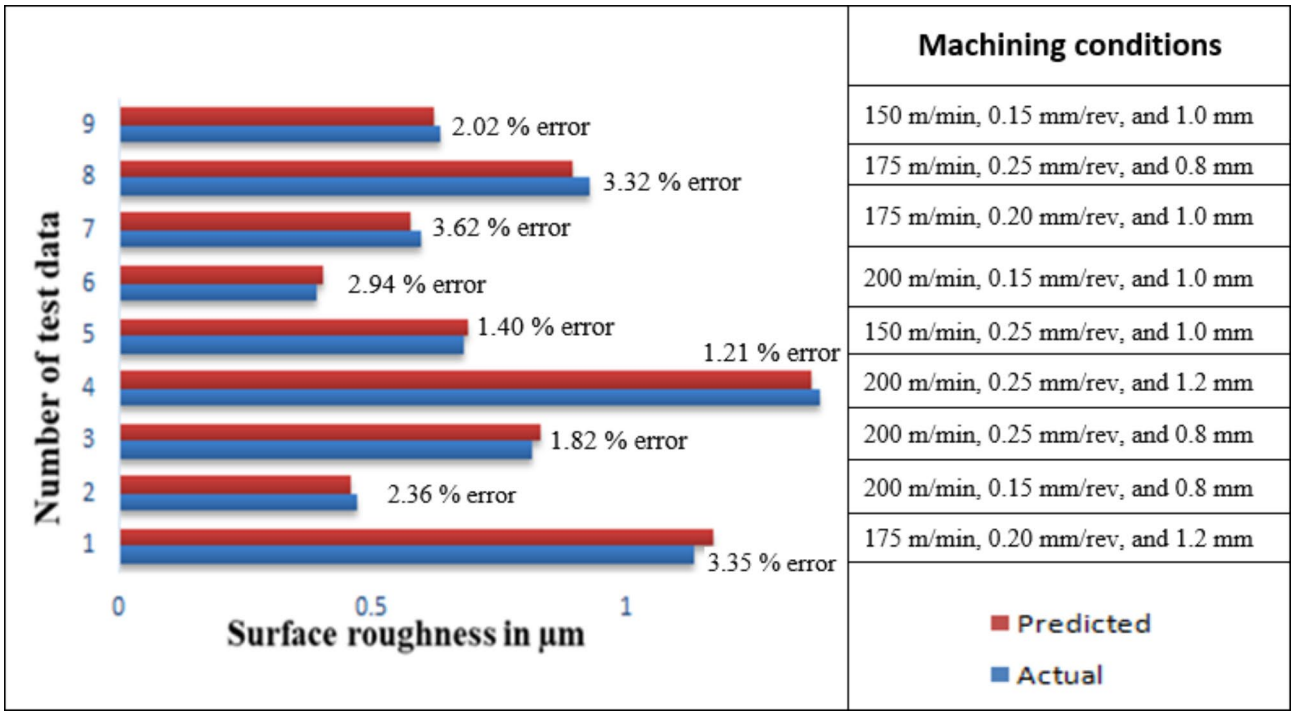

Fig. 8. Comparison of R_a values between stylus measured and predicted for RBFNN model 6 for randomly selected test data.

Sl. no	Experimental R_a	Predicted R_a	Error %
1	0.3808	0.3863	1.44
2	0.3716	0.3823	2.87
3	0.5194	0.5038	3.00
4	0.4406	0.4553	3.33
5	0.4144	0.4070	1.78

Table 14. Results obtained from validation data.

Width	Prediction accuracy (%)		Average MSE
	Training	Test	
0.10	98.91	96.24	0.018
0.15	100	97.12	0.017
0.20	98.91	96.51	0.019
0.25	96.53	94.44	0.018

Table 15. Validation performance of RBFNN model 6 using data captured in the proposed approach.

Sl. no	Experimental R_a	Predicted R_a	Error %
1	5.2836	5.1117	3.25
2	7.4298	7.5991	2.28
3	5.4637	5.3261	2.52
4	6.8916	6.7776	1.65

Table 16. Results obtained for shaped images.

on training and test data to compare of DTCWT image processing methods and features extracted using GLCM. The following are the significant conclusions which can be made from the presented work:

1. DTCWT image fusion is a novel feature generation technique for extracting GLCM features in turned surface images because of its better directionality and shift invariance properties.
2. The PSO algorithm effectively calculates the weights based on an objective function that represents the edge details and contrast of the fused image. This improves the fused image's clarity and quality.
3. The RBFNN model based on DTCWT Image fusion with PSO based on PCA features (model 6) gives the best results with 100% prediction accuracy for training data and 99.13% for test data. From the validation test, it is observed that there has been good agreement between the actual stylus measured R_a and predicted R_a from the proposed work, with a minimum error of 1.44% for randomly selected data.
4. Validation experiments based on shaping operation provide good prediction accuracy of 100% for training data and 97.12% for test data, with an error rate of less than 4% between stylus measured R_a and predicted R_a which are affordable in an industrial environment. Further, a comparison of the performance of the proposed method by the authors with the work carried out by the authors earlier and related work, establishes the strength of this method in surface roughness modeling and prediction using wavelet transform and ANN.

DTCWT image fusion with PSO and GLCM feature extraction can effectively model and predict the surface roughness of Ti-6Al-4 V turned images, supporting industry efforts for effective non-contact measurement of the surface roughness of machined surfaces.

Data availability

All data generated or analysed during this study are included in this published article.

Received: 1 April 2024; Accepted: 3 October 2024
Published online: 16 November 2024

References

1. Lu, E., Ren, W., Dai, H. & Zhu, X. Investigations on electromagnetic wave scattering simulation from rough surface: Some instructions for surface roughness measurement based on machine vison. *Precis. Eng.* **82**, 156–168. https://doi.org/10.1016/j.precisioneng.2023.03.017 (2023).
2. Dedeakayoğulları, H., Kaçal, A. & Keser, K. Modeling and prediction of surface roughness at the drilling of SLM-Ti6Al4V parts manufactured with pre-hole with optimized ANN and ANFIS. *Measurement* **203**, 112029. https://doi.org/10.1016/j.measurement.2022.112029 (2022).
3. Zhao, S. et al. Evaluation of wear mechanism between TC4 titanium alloys and self-lubricating fabrics. *Wear* **512–513**, 204532. https://doi.org/10.1016/j.wear.2022.204532 (2023).
4. Liu, Y. et al. Machine vision based condition monitoring and fault diagnosis of machine tools using information from machined surface texture: A review. *Mech. Syst. Signal Process.* **164**, 108068. https://doi.org/10.1016/j.ymssp.2021.108068 (2022).
5. Kumar, V. & Sudheesh-Kumar, C. P. Investigation of the influence of coloured illumination on surface texture features: A Machine vision approach. *Measurement* **152**, 107297. https://doi.org/10.1016/j.measurement.2019.107297 (2020).
6. Morala-Argüello, P., Barreiro, J. & Alegre, E. A evaluation of surface roughness classes by computer vision using wavelet transform in the frequency domain. *Int. J. Adv. Manuf. Technol.* **59**, 213–220. https://doi.org/10.1007/s00170-011-3480-6 (2012).
7. Rifai, A. P. et al. Evaluation of turned and milled surfaces roughness using convolutional neural network. *Measurement* https://doi.org/10.1016/j.measurement.2020.107860 (2020).
8. Chui, C. K. *An Introduction to Wavelets* (Academic Press, 1992). https://doi.org/10.2307/2153134.
9. Hirsch, M., Sra, S., Schölkopf, B., & Harmeling, S. Efficient filter flow for space variant multi frame blind deconvolution. In *CVPR* 607–614 (2010). https://doi.org/10.1109/CVPR.2010.5540158.
10. Lo, E. H. S., Pickering, M. R., Frater, M. R. & Arnold, J. F. Image segmentation from scale and rotation invariant texture features from the double dyadic dual-tree complex wavelet transform. *Image Vis. Comput.* **29**(1), 15–28. https://doi.org/10.1109/ICASSP.2007.365981 (2011).
11. Kingsbury, N. G. Complex wavelets for shift invariant analysis and filtering of signals. *J. Appl. Comput. Harmon. Anal.* **10**(3), 234–253. https://doi.org/10.1006/acha.2000.0343 (2001).
12. Zheng, Q., Chen, G. & Jiao, A. Chatter detection in milling process based on the combination of wavelet packet transform and PSO-SVM. *Int. J. Adv. Manuf. Technol.* **120**(1), 1237–1251. https://doi.org/10.1007/s00170-022-08856-3 (2022).
13. Rahul, V. M., Balaji, V. & Narendranath, S. Optimization of wire-EDM process parameters for Ni–Ti–Hf shape memory alloy through particle swarm optimization and CNN-based SEM-image classification. *Results Eng.* **18**, 101141. https://doi.org/10.1016/j.rineng.2023.101141 (2023).
14. Zhao, H. et al. Research on intelligent prediction of surface roughness in cutting 42CrMo steel by using particle swarm optimization-based support vector machine. *Int. J. Precis. Eng. Manuf.* https://doi.org/10.1007/s12541-024-01077-6 (2024).
15. Chang, Y. et al. PCB defect detection based on PSO-optimized threshold segmentation and SURF features. *Signal Image Video Process.* **18**(5), 4327–4336. https://doi.org/10.1007/s11760-024-03075-7 (2024).
16. Luis-Pérez, C. J. Multi-objective optimization of electrical discharge machining parameters using particle swarm optimization. *Appl. Soft Comput.* **153**, 111300. https://doi.org/10.1016/j.asoc.2024.111300 (2024).
17. Tao, J., Li, S., & Yang, B. Multimodal image fusion algorithm using dual-tree complex wavelet transform and particle swarm optimization. In *ICIC 2010. CCIS* Vol. 93, 296–303 (2010). https://doi.org/10.1007/978-3-642-14831-6_40.
18. Padmavathi, K., Asha, C. S. & Maya, V. Karki: A novel medical image fusion by combining TV-L1 decomposed textures based on adaptive weighting scheme. *Eng. Sci. Technol.* https://doi.org/10.1016/j.jestch.2019.03.008 (2019).
19. Vishwanatha, J. S., Srinivasa Pai, P., & D'Mello, G. Wavelet transform based evaluation of surface images in high speed turning of Ti-6Al-4V. *Indian J. Adv. Chem. Sci.* 152–156 (2016).
20. Gadelmawla, E. S. A vision system for surface roughness characterization using the gray level co-occurrence matrix. *NDT&E Int.* **37**, 577–588. https://doi.org/10.1016/j.ndteint.2004.03.004 (2004).
21. Bhat, N. N. et al. Tool condition monitoring by SVM classification of machined surface images in turning. *Int. J. Adv. Manuf. Technol.* **83**, 1487–1502. https://doi.org/10.1007/s00170-015-7441-3 (2016).
22. Lee, B. Y., Yu, S. F. & Juan, H. The model of surface roughness inspection by vision system in turning. *Mechatronics* **14**, 129–141. https://doi.org/10.1016/S0957-4158(02)00096-X (2004).

23. Kohli, A. & Dixit, U. S. A. Neural network based methodology for prediction of surface roughness in turning process. *Int. J. Adv. Manuf. Technol.* **25**(1–2), 118–129. https://doi.org/10.1007/s00170-003-1810-z (2005).
24. Ravi Keerthi, C., SrinivasaPai, P. & Vishwanatha, J. S. Wavelet transform based recognition of machined surfaces using computer vision. *Appl. Mech. Mater.* **592–594**, 801–805. https://doi.org/10.4028/www.scientific.net/AMM.592-594.801 (2014).
25. Tsai, D.-M., Chen, J.-J. & Chert, J.-F. A vision system for surface roughness assessment using neural networks. *Int. J. Adv. Manuf. Technol.* **14**, 412–422 (1998).
26. D'Mello, G., Srinivasa Pai, P. & Puneet, N. P. Surface roughness prediction in high speed turning of Ti-6Al-4V: A comparison of techniques. *Mater. Sci. Eng.* **376**, 012115. https://doi.org/10.24874/ti.2018.40.03.12 (2018).
27. Garg, S. et al. Evaluation of the performance of back propagation and radial basis function neural networks in predicting the drill flank wear. *Neural Comput. Appl.* **16**, 407–417. https://doi.org/10.1007/s00521-006-0065-7 (2007).
28. Wang, H., Lu, H., Alelaumi, S. M. & Yoon, S. W. A wavelet-based multi-dimensional temporal recurrent neural network for stencil printing performance prediction. *Robot. Comput. Integr. Manuf.* **71**, 102129. https://doi.org/10.1016/j.rcim.2021.102129 (2021).
29. Grochała, D., Grzejda, R., Parus, A. & Berczyński, S. The wavelet transform for feature extraction and surface roughness evaluation after micromachining. *Coatings* **14**(2), 210. https://doi.org/10.3390/coatings14020210 (2024).
30. Arun, P. S., Sahare, S. A. & Gopi, V. P. Rescownet: A deep convolutional neural network with residual learning based on dt-cwt for despeckling optical coherence tomography images. *Optik* **284**, 170924. https://doi.org/10.1016/j.ijleo.2023.170924 (2023).
31. Zhou, Y., Cao, R., Zhang, A. & Li, P. An interference mitigation method for FMCW radar based on time-frequency distribution and dual-domain fusion filtering. *Sensors* **24**(11), 3288. https://doi.org/10.3390/s24113288 (2024).
32. Yan, T., Zhang, D., Wang, Y., Sun, H., Tang, Y., & Yang, Y. Improved algorithm of TOF image fusion based on DTCWT. In *International Conference on Image Processing and Artificial Intelligence (ICIPAI 2024)* Vol. 13213, 12–20 (2024). SPIE.
33. Bhonsle, D. Denoising of digital images using wavelet-based thresholding techniques: A comparison. In *Cognitive Behavior and Human Computer Interaction Based on Machine Learning Algorithm*, 85–115 (2021). https://doi.org/10.1002/9781119792109.ch4
34. Abdulla, S. M. & Jayakumari, J. Improving time–frequency sparsity for enhanced audio source separation in degenerate unmixing estimation technique algorithm. *J. Control Dec.* **9**(4), 502–515. https://doi.org/10.1080/23307706.2022.2074900 (2022).
35. Papandrea, P. J., Frigieri, E. P., Maia, P. R., Oliveira, L. G. & Paiva, A. P. Surface roughness diagnosis in hard turning using acoustic signals and support vector machine: A PCA-based approach. *Appl. Acoust.* **159**, 107102. https://doi.org/10.1016/j.apacoust.2019.107102 (2020).
36. Liu, Y. et al. Machine vision based condition monitoring and fault diagnosis of machine tools using information from machined surface texture: A review. *Mech. Syst. Signal Process.* **164**, 108068. https://doi.org/10.1016/j.ymssp.2021.108068 (2022).
37. Khan, S. U. et al. A machine learning-based approach for the segmentation and classification of malignant cells in breast cytology images using gray level co-occurrence matrix (GLCM) and support vector machine (SVM). *Neural Comput. Appl.* https://doi.org/10.1007/s00521-021-05697-1 (2022).
38. Prasad, G., Gaddale, V. S., Kamath, R. C., Shekaranaik, V. J. & Pai, S. P. A study of dimensionality reduction in GLCM feature-based classification of machined surface images. *Arab. J. Sci. Eng.* **49**(2), 1531–1553. https://doi.org/10.1007/s13369-023-07854-1 (2024).
39. Natarajan, U., Palani, S. & Anandampilai, B. Prediction of surface roughness in milling by machine vision using ANFIS. *Comput. Aided Des. Appl.* **9**(3), 269–288. https://doi.org/10.3722/cadaps.2012.269-288 (2013).
40. Mallat, S. G. A theory for multiresolution signal decomposition: The wavelet representation. *IEEE Trans. PAMI* **11**, 674–693. https://doi.org/10.1109/34.192463 (1989).
41. Selesnick, I., Baraniuk, R. & Kingsbury, N. C. The dual-tree complex wavelet transform. *IEEE Signal Process. Mag.* **22**(6), 123–151. https://doi.org/10.1109/MSP.2005.1550194 (2005).
42. Yang, P. Feature extraction using dual-tree complex wavelet transform and gray Level co-occurrence matrix. *Neurocomputing* **197**, 212–220. https://doi.org/10.1016/j.neucom.2016.02.061 (2016).
43. Farhat I.A., & El-Hawary M.E., Short-term hydro-thermal scheduling using an improved bacterial foraging algorithm. In *IEEE Conference on Electrical Power & Energy* 1–5 (2009). https://doi.org/10.1109/EPEC.2009.5420913.
44. Kennedy J. & Eberhart, R. Particle swarm optimization. In *Proceedings of IEEE International Conference on* Neural *Networks Perth Australia*, vol. 4 1942–1948 (1995). https://doi.org/10.1109/ICNN.1995.488968.
45. Prakash, J., Singh, P. K. & Kishor, A. Integrating fitness predator optimizer with multi-objective PSO for dynamic partitional clustering. *Progress Artif. Intell.* **8**, 83–99. https://doi.org/10.1007/s13748-018-0157-5 (2019).
46. Timothee, C., Florence, B., Jianbo, S. Spectral segmentation with multiscale graph decomposition. In *Proc. of Computer Vision Pattern Recognition* 1124–1131 (2005). https://doi.org/10.1109/CVPR.2005.332.
47. Piella, G., Heijmans, H. A new quality metric for image fusion. In *Proc. of International Conference on Image Processing* (2003). https://doi.org/10.1109/ICIP.2003.1247209
48. Das, A. K., Pratihar, B. & Pratihar, D. K. Evolving fuzzy reasoning approach using a novel nature-inspired optimization tool. *Expert Syst. Appl.***170**, 114577. https://doi.org/10.1016/j.eswa.2021.114577 (2021).
49. GC, M. P., Krishna, P., Parappagoudar, M. B. & Vundavilli, P. R. Multi-objective optimization of squeeze casting process using evolutionary algorithms. *Int. J. Swarm Intell. Res. (IJSIR).* **7** (1), 55–74. https://doi.org/10.4018/IJSIR.2016010103 (2016).
50. Haralick, R. M. et al. Textural features for image classification. *IEEE Trans. Syst. Man Cybern. SMC* **3**, 610–621. https://doi.org/10.1109/TSMC.1973.4309314 (1973).
51. Albregtsen, F. Statistical texture measures computed from Gray Level co-occurrence matrices. Image Processing Laboratory. *Department Inf. Univ. Oslo* (2008). https://www.researchgate.net/publication/255652481_Statistical_Texture_Measures_Computed_from_Gray_Level_Coocurrence_Matrices
52. Hotelling, H. Analysis of a complex of statistical variables into principal components. *J. EducPsychol.* **24**, 417–441. https://doi.org/10.1037/h0071325 (1993).
53. Gupta, M. Investigation of surface roughness and MRR for turning of UD-GFRP using PCA and Taguchi method. *Eng. Sci. Technol. Int* **J18**(1), 70–81. https://doi.org/10.1016/j.jestch.2014.09.006 (2015).
54. Haykin, S. Neural networks a comprehensive foundation, 2nd edn (1999) https://www.pearson.com/us/higher-education/product/Haykin-Neural-Networks-A-Comprehensive-Foundation-2nd-Edition/9780132733502.html.
55. Mehera, B., Agrawala, S., Pandaa, R. & Abraham, A. A survey on region based image fusion methods. *Inf. Fusion* **48**, 119–132. https://doi.org/10.1016/j.inffus.2018.07.010 (2019).

Acknowledgements

The authors extend their appreciation to the Deanship of Research and Graduate Studies at King Khalid University for funding this work through Large Research Project under grant number RGP2/294/45.

Author contributions

Vishwanatha J S. Srinivasa Pai and Grynal D'Mello .L. Sampath Kumar. Wrote the main manuscript and Raghavendra Bairy. Madeva Nagaral and Channa Keshava Naik N. Contributed for Analysis and validation. Venkatesh T Lamani. Chandrashekar A. and M. Yunus Khan. Prepared the figures and Tables. All other authors reviewed the manuscript.

Declarations

Competing interests
he authors declare no competing interests.

Additional information
Correspondence and requests for materials should be addressed to M.N., N.C.K.N. or W.A.K.

Reprints and permissions information is available at www.nature.com/reprints.

Publisher's note Springer Nature remains neutral with regard to jurisdictional claims in published maps and institutional affiliations.